

Polarization Effects of Confocal Raman Microspectrometry of Crystal Powders Using Interactive Self-Modeling Analysis

Yann Batonneau,[†] Claude Brémard,^{*,†} Jacky Laureyns,[†] Jean-Claude Merlin,[†] and Willem Windig^{‡,§}

Laboratoire de Spectrochimie Infrarouge et Raman UMR-CNRS 8516, Centre d'Etudes et de Recherches Lasers et Applications, Bât. C5 Université des Sciences et Technologies de Lille, 59655 Villeneuve d'Ascq Cedex, France, and Imaging Materials and Media, Research & Development, Eastman Kodak Company, Rochester, New York 14650-2132

Received: July 30, 2002; In Final Form: November 26, 2002

The collection by confocal Raman microspectrometry in the motorized point-by-point scanning mode of crystalline samples with heterogeneity larger than the spatial resolution ($\sim 1\ \mu\text{m}$) generates large amounts of useable Raman spectral data. The present selected examples of fine, medium, and coarse crystal powders (anhydrite, CaSO_4 ; calcite, CaCO_3 ; gypsum, $\text{CaSO}_4 \cdot 2\text{H}_2\text{O}$; and $(\text{NH}_4)_2\text{SO}_4$) treated by the new Simplisma method combining conventional and second derivative data demonstrate the main role of the crystal size on the number and shape of the resolved spectra. With fine crystal powders (size less than $0.5\ \mu\text{m}$), well-known powder Raman spectrum characteristics of each compound were extracted. These spectra were often superimposed on a weak baseline. With medium and coarse crystal powders (size more than $1\ \mu\text{m}$), several significant spectra were extracted for each pure crystalline compound. These spectra were found to be analogous to the polarized spectra previously obtained with oriented large single crystal and were attributed to the several scattering contributions according to the symmetry of the several vibrational modes. The band splittings by the static and dynamic crystal effects can be resolved by the Simplisma approach using the pure variable concept according to the width of the splitting depending on the crystal. These results were explained by theoretical equations deduced from the Raman tensor elements and orientational functions of the crystal-fixed coordinates with respect to the space-fixed coordinates. These findings could provide accurate assignment of the resolved spectra extracted by the Simplisma approach from mixtures with large heterogeneities and can provide meaningful applications to Raman imaging of environmental and material samples.

Introduction

The use of Raman scattering spectroscopy in conjunction with a confocal microscope offers a unique combination of molecular chemical, physical characterization, and spatial resolution at the micrometer scale. Raman microspectrometry is widely used to analyze map and image properties in one, two, or three dimensions of many types of samples with *in situ* conditions and without any specific preparation. It was already shown that polarized Raman microspectrometry using linearly polarized laser excitation is very useful to distinguish vibrational modes of small crystals according to their symmetry as well as local molecular orientation in liquids, crystals, and polymers. Recently, confocal Raman microspectrometry was presented as a promising means of molecular microanalysis and mapping of environmental samples (soils, sediments, or atmospheric dusts) with *in situ* conditions. Unfortunately, the large heterogeneity (less than $0.5\ \mu\text{m}$) at the level of the individual particle (less than $5\ \mu\text{m}$) of environmental samples generates severe overlap of spectral information to obtain pure component spectra and concentrations. For cases where spectral mixture data are available without either pure component spectra or concentration

profiles of pure components, a wide variety of self-modeling mixture analysis tools are available.^{1,2} The Simplisma (Simple-to-use interactive self-modeling mixture analysis) approach is different in that it is not based on principal component analysis and it is interactive.^{3,4} The interactivity is important to resolve data sets dealing with environmental chemistry where it is not possible to obtain replicate samples when trouble-shooting: user interaction based on its spectroscopic knowledge is necessary to avoid meaningless problems. When highly overlapping spectral features and/or baselines are present in the spectra, second derivative spectra can be used to resolve the data properly.^{5–8} This approach uses pure spectra as a first estimate and derives pure variables from the resolved contribution profiles.

Simplisma has been described for a variety of applications including: (i) Raman spectra of a time-resolved reaction of tetramethyl orthosilicate,^{3,9} hydrogen peroxide activation by nitriles,¹⁰ photooxidation products of lead sulfide crystals,¹¹ imaging of dust particles emitted by smelters,^{12,13} and aromatic compounds occluded in zeolites;^{14–16} (ii) FTIR microscopy of a polymer laminate;^{3,6–9} (iii) pyrolysis mass spectral data of plant materials;⁴ (iv) time-resolved mass spectral data of photographic color-coupling compounds;^{9,17} (v) infrared spectra of mixtures of solvents,^{5,18} polymers,^{19,20} monitoring of powder blending,²¹ and water;²² (vi) diffuse reflectance UV–vis spectra of zeolites,^{23,24} metal oxide catalysts,²⁵ and polynucleotides;²⁶

* To whom correspondence should be addressed. Fax: 0033(0)3 20 43 67 55. E-mail: claude.bremard@univ-lille1.fr.

[†] Bât. C5 Université des Sciences et Technologies de Lille.

[‡] Eastman Kodak Company.

[§] Present address: Eigenvector Research, Inc., 830 Wapato Lake Road, Manson WA 98831.

(vii) time-resolved absorption spectra of short-lived transient species of aromatic compounds;²⁷ (viii) fluorescence spectra of fulvic acids,^{28–30} leaf litter,³¹ and natural organic matter from water;³² (ix) ion mobility spectra;^{33,34} and (x) X-ray photoelectron spectra of blends of poly(vinyl chloride) and poly(methyl methacrylate).³⁵

A recent paper described a new Simplisma approach in which both the conventional spectra and the second derivative spectra are used, the former for pure variables of wide bands and the latter for pure variables of narrow peaks, overlapping with wide bands. This new approach is able to properly resolve spectra with wide bands and narrow peaks and minimizes baseline problems by resolving them as separate components of samples.¹³ This finding is particularly interesting for Raman mapping of environmental samples where narrow Raman scattering peaks are often superimposed with large backgrounds induced by fluorescence emission and diffuse reflectance of powdered samples.

Nevertheless, in the Simplisma approach, it is assumed that the components exhibit isotropic Raman scattering. This hypothesis is correct for isotropic samples or fine crystal powders with random orientation. In contrast, this hypothesis is not true for crystallized compounds with crystal size in the order of or larger than the spot size of the laser beam focused on the sample (1 μm). The Raman scattered light intensity corresponding to Raman active vibrational transitions in crystals is determined by selection rules and orientation of crystals with respect to the propagation and polarization orientation of both exciting laser and collected Raman scattering light. The effect of large NA objective used to focus the laser beam and to collect the scattered light was evaluated previously.³⁶ In the present work, we are applying polarized Raman microspectrometry to collect big-sized spectral data of coarse, medium, and fine crystal powders, which are of spectroscopic and environmental interest. The crystal structures, polarized Raman spectra, and optical properties of CaSO_4 (anhydrite), CaCO_3 (calcite), $\text{CaSO}_4 \cdot 2\text{H}_2\text{O}$ (gypsum), and $(\text{NH}_4)_2\text{SO}_4$ are well-documented, and these compounds are often found in atmospheric and soil particles with large heterogeneity in crystal size.

It is emphasized herein on the data processing of the numerous spectra using the Simplisma approach because the intensities of the variables are assumed not to be due to concentrations but to orientation of individual crystals with respect to space-fixed coordinates. The initial aim of this work is the discrimination between powder spectra and polarized Raman spectra based on the elements of the Raman scattering tensors of vibrational modes. This purpose is to provide an extensive explanation spectra of crystalline samples with large heterogeneity resolved by the Simplisma approach as well as Raman imaging applications. However, the present results can provide meaningful applications to molecular orientation mapping of polymeric^{37,38} or liquid crystal materials with severe spectral overlaps.^{39–41}

Experimental Section

Crystal Powders, Morphology, and Optical Properties.

Some natural crystals of CaSO_4 were ground in a mortar and used as obtained (crystallite size less than 2 μm).

Synthetic CaCO_3 as fine, medium, and coarse crystal powders was used as obtained. CaCO_3 : Prolabo, 95%, particle size less than 1 μm being aggregates of many crystallites; Prolabo, 95%, crystal size $\sim 1 \mu\text{m}$ calcium carbonate; Sigma, ACS reagent, 99.3%, crystal size $\sim 7 \mu\text{m}$. The individual crystal morphology was rhombohedral. Calcite is an uniaxial strong birefringent

material with ordinary (1.6584) and extraordinary (1.4865) indices in the visible wavelength region.⁴²

Synthetic gypsum ($\text{CaSO}_4 \cdot 2\text{H}_2\text{O}$, Prolabo, 99.99%, particle size less than 15 μm being aggregates of many crystallites less than 1 μm) was used as obtained. Gypsum is a biaxial, weakly birefringent material with 1.5262, 1.5285, and 1.5355 index values in the visible wavelength region.⁴³

Synthetic $(\text{NH}_4)_2\text{SO}_4$ (Merck, 99.5%, particle size less than 15 μm being aggregates of many needle-shaped crystallites) was used as obtained.

Apparatus and Spectra Collection. Raman microspectrometric measurements were carried out with a LabRAM confocal scanning spectrometer manufactured by Instruments S. A. (Dilor, France). It was coupled confocally with an Olympus high-stability BX 40 microscope. A liquid nitrogen-cooled CCD (Jobin-Yvon, 2048 \times 512 pixels) was used for detection, allowing simultaneous spectral dispersion by a 1800 grooves mm^{-1} holographic grating over a wide wavenumber range of more than 1000 cm^{-1} in the spectral region of interest. Raman backscattering was excited with a 632.8 nm excitation wavelength supplied by an internal, air-cooled, linearly polarized helium–neon laser. Laser power delivered at the sample was 8 mW (without polarizer and analyzer in the beam path) and could be monitored via a filter wheel with the optical densities 0.3, 0.6, 1, 2, 3, and 4 (Figure 1). An Olympus 100 \times objective, numerical aperture (NA) = 0.90 was used. The spot size of the laser focused by the 100 \times objective at the sample was estimated to be less than 1 μm in size. Except when noted, the Stokes Raman spectra were recorded over the 105–1185 cm^{-1} spectral range. The spectrometer calibration was verified using the Raman lines of silicon. This resulted in an accuracy of less than $\pm 1 \text{ cm}^{-1}$. A color camera was used to feed a signal to a video monitor and thus provided an optical view of the samples. TV images obtained could be digitalized through a Vitec video card. The microscope stage was XY-motorized and computer-controlled for point by point scanning imaging with 0.1 μm resolution, 1 μm reproducibility, and 90 \times 60 mm^2 spatial range. Because of the roughness of the crystallites, a piezoelectric Z actuator (Physical Instruments) for automatic focusing of the exciting beam at each point was used. A PC with Labspec software piloted and controlled the spectrometer, the filter wheel, the slit, and the confocal hole apertures. Furthermore, it accomplished the synchronization of stage movement, autofocus of the laser beam onto the crystallites surfaces, and data collection. As can be seen in Figure 1, a high-aperture microscope objective and a Notch Filter intervene in the light paths of both the excitation and the Raman-scattered radiations. The latter optical element, responsible for the relative compactness of the instrument, acts as a mirror toward the excitation light whereas it eliminates the elastic and low-frequency inelastic contributions of the scattered light collected by the microscope objective. A rotating polarizer (half-wave plate) was placed in the laser path in order to discriminate between X and Y exciting polarized light (Figure 1). The scattered light was analyzed by positioning an analyzer (Polaroid film) vertically (X) or horizontally (Y) in front of the entrance slit of the spectrometer. During the polarization measurements presented here, the analyzer was set fixed in the vertical position (X). No scrambler was added immediately after the analyzer. A slit aperture (viz. 120 or 150 μm) as small as possible was used to ensure an optimal spectral width (4.7 and 5.9 cm^{-1} , respectively) as a maximum resolution, which is of major importance when polarization measurements are performed. The hole aperture was set to 200 or 300 μm to ensure a minimum depth of analysis,

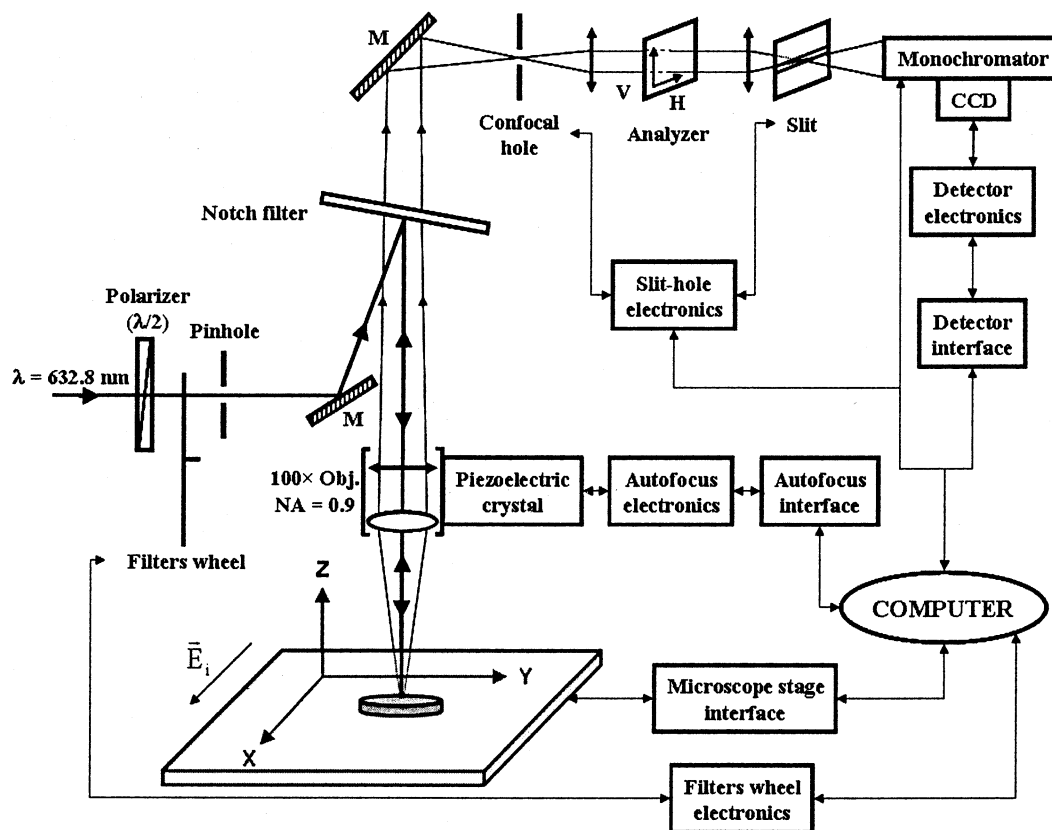


Figure 1. Experimental setup for the polarized Raman microspectrometric measurements. The source electric field vector shown (\vec{E}_i) corresponds to this of the laser at the sample.

which is of major importance to avoid polarization scrambling with birefringent materials (from ca. 0.8 to 0.9 μm at the exciting source wavelength used, depending on the optical indices of compounds under study). The crystal powder was spread on a microscope glass strip without any further preparation and mounted on the XY microscope stage. The data acquisition consisted in recording many spectra in point-by-point mapping mode with 1 μm as a minimum step, one accumulation, and 10 s spectrum acquisition time.

Crystalline Structure, Crystal Faces, and Raman Active Vibrational Modes. *CaSO₄*. The anhydrite crystalline structure belongs to D_{2h}^{17} space group (*Cmcm*) with two formula units per primitive cell ($Z = 2$). Anhydrite cleaves readily along the faces {100}, {010}, and {001}. The reduced representation of the 18 Raman active fundamentals is given by

$$6A_g + 5B_{1g} + 2B_{2g} + 5B_{3g} \quad (1)$$

CaCO₃. The space group of *CaCO₃* is D_{3d}^6 ($R\bar{3}/c$) with $Z = 2$. The most stable face is {10 $\bar{1}$ 4} or equivalent faces with rhombohedral crystal morphology. The reduced representation of the five Raman active fundamentals is

$$A_{1g} + 4E_g \quad (2)$$

CaSO₄·2H₂O. The space group of gypsum is C_{2h}^6 (*C2/c*) with $Z = 2$. The well-formed faces are {010}, {001}, and {111}. The reduced representation of the Raman active fundamentals is

$$17A_g + 19B_g \quad (3)$$

Ammonium Sulfate ((NH₄)₂SO₄). The (NH₄)₂SO₄ crystalline structure belongs to the D_{2h}^{16} space group (*Pnma*) with $Z = 4$.

The crystal exhibits well-defined {001} faces. Ammonium ions NH₄⁺ are crystallographically nonequivalent, and the reduced representation of the Raman active fundamentals is given by

$$27A_g + 27B_{1g} + 18B_{2g} + 18B_{3g} \quad (4)$$

Polarized Raman Microspectrometry of Crystals. An insight into the theory of polarized Raman scattering using highly focused exciting and scattered light is summarized in this section. An expression for the scattering intensity in a Raman microprobe instrument can be written in the following form:⁴⁴

$$I_s = K \int_V \int_{\Omega} |\vec{E}_e \cdot \alpha_{XYZ} \cdot E_s|^2 d\Omega \cdot dV \quad (5)$$

with $K = 4\pi^2\gamma^2 I_e (\bar{\nu}_0 - \Delta\bar{\nu})^4$, where $\gamma = 1/137$, I_e is the exciting intensity, $\bar{\nu}_0$ and $\Delta\bar{\nu}$ are the wavenumbers of the exciting and Raman-shifted radiation, respectively, E_e (\vec{E}_e) is the electric vector (the transpose of the electric vector) of the exciting light, E_s is the electric vector of the scattered light, α_{XYZ} is the Raman tensor of the sample system in the space-fixed coordinates XYZ (cf. Figure 2a), V is the total scattering volume, and Ω is the solid angle defined by the angular semiaperture of the objective.

Elements of the Raman tensor α_{XYZ} are noted as follows with respect to the space-fixed XYZ coordinates:

$$\alpha_{XYZ} = \begin{pmatrix} \alpha_{XX} & \alpha_{XY} & \alpha_{XZ} \\ \alpha_{YX} & \alpha_{YY} & \alpha_{YZ} \\ \alpha_{ZX} & \alpha_{ZY} & \alpha_{ZZ} \end{pmatrix} \quad (6)$$

Equation 5 has previously been evaluated for the case of a linearly polarized source focused by a large NA objective and collected by the same objective, and it was revisited recently.³⁷

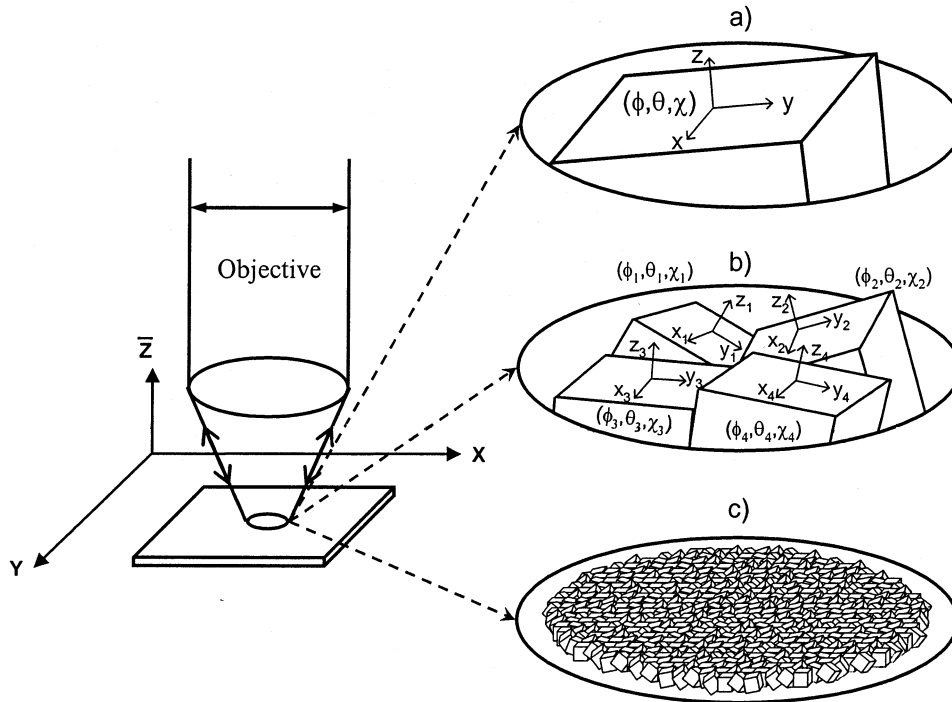


Figure 2. Modeled representation of the solid sample surface illuminated by the excitation source XYZ defines the space-fixed coordinate system. (a) Case where a unique cleavage surface is illuminated. xyz defines the crystal-fixed coordinate system, which is linked to XYZ by the Euler angles $(\theta\phi\chi)$ as defined in ref 48. (b) Case where several cleavage surfaces are illuminated by the microscope objective in the same time. $(x_i, y_i, z_i)_{1 \leq i \leq 4}$ defines the respective crystal-fixed coordinate systems, which are linked to XYZ by the Euler angles $(\theta_i\phi_i\chi_i)_{1 \leq i \leq 4}$ as defined in ref 48, respectively. (c) Case where a great number of cleavage surfaces are illuminated by the microscope objective in the same time.

If the axis of the incident and scattering cone is taken to be the Z -axis and the incident light is polarized in the X direction, eq 5 becomes

$$I = (\alpha_{XX}^2 A + \alpha_{XY}^2 B + \alpha_{XZ}^2 B) \cdot (2C_0 + C_2) + (\alpha_{YX}^2 A + \alpha_{YY}^2 A + \alpha_{YZ}^2 B) \cdot C_2 + (\alpha_{ZX}^2 A + \alpha_{ZY}^2 A + \alpha_{ZZ}^2 B) \cdot 4C_1 \quad (7)$$

The respective values of coefficients C_0 , C_1 , and C_2 , concerning the focused exciting light and A and B for collected light, were previously calculated for different aperture objectives and several mean refractive indices (see refs 36 and 44–47). The use of an analyzer fixed in the X direction suppresses the α_{XY} , α_{YY} , and α_{ZY} elements and reduces eq 7 to

$$I_{YX} = (\alpha_{XX}^2 A + \alpha_{XZ}^2 B) \cdot C_2 + (\alpha_{YX}^2 A + \alpha_{YZ}^2 B) \cdot (2C_0 + C_2) + (\alpha_{ZX}^2 A + \alpha_{ZZ}^2 B) \cdot 4C_1 \quad (8)$$

This I_{YX} configuration was chosen to obtain a good signal-to-noise ratio with a reasonable integration time of the detector. It should be noted that the I_{XX} configuration provides analogous results. With strictly parallel exciting and scattered lights, eq 8 can be reduced to $I_{YX} \propto \alpha_{YX}^2$. The polarizability tensor in the space-fixed coordinates XYZ relates to the Raman polarizability tensor in the crystal-fixed coordinates xyz by

$$\alpha_{XYZ} = \tilde{\mathbf{R}} \cdot \alpha_{xyz} \cdot \mathbf{R} \quad (9)$$

where \mathbf{R} (respectively, $\tilde{\mathbf{R}}$) is the rotation matrix (and its transpose) previously defined with respect to Euler angles (ϕ, θ, χ) .⁴⁸ The expressions of the Raman tensor elements α_{IJ} in the laboratory frame in terms of polarizability Raman tensor

elements α_{ij} and Eulerian angle functions were previously detailed in ref 39, for example

$$\alpha_{YX} = \frac{1}{4}(2\alpha_{zz} - \alpha_{xx} - \alpha_{yy}) \cdot p_1 + \frac{1}{4}(\alpha_{xx} - \alpha_{yy}) \cdot p_2 - \frac{1}{2}\alpha_{xy} \cdot p_3 + \alpha_{xz} \cdot p_4 - \alpha_{yz} \cdot p_5 \quad (10)$$

The p_1 , p_2 , p_3 , p_4 , and p_5 orientational functions of the Eulerian angles are³⁹

$$p_1 = \sin 2\phi \cdot \sin^2 \theta$$

$$p_2 = \sin 2\phi \cdot (1 + \cos^2 \theta) \cdot \cos 2\chi + 2\cos 2\phi \cdot \cos \theta \cdot \sin 2\chi$$

$$p_3 = \sin 2\phi \cdot (1 + \cos^2 \theta) \cdot \sin 2\chi - 2\cos 2\phi \cdot \cos \theta \cdot \cos 2\chi$$

$$p_4 = \sin \theta \cdot (\sin 2\phi \cdot \cos \theta \cdot \cos \chi + \cos 2\phi \cdot \sin \chi)$$

$$p_5 = \sin \theta \cdot (\sin 2\phi \cdot \cos \theta \cdot \sin \chi - \cos 2\phi \cdot \cos \chi)$$

The use of a high aperture objective induces in theory the use of eq 8 where all of the α_{IJ} tensor elements were replaced by crystal tensor elements α_{ij} and the corresponding p_k orientational functions detailed in the ref 39. With the $\times 100$ objective, NA 0.9, the correction coefficients have the relative following values: $C_0 > 10C_1 > 300C_2$ and $A > 10B$ with a 1.5 optical index. It should be noted that these corrections do not take the birefringence polarization scrambling into account. This later effect was reduced to minor contribution in our confocal experimental conditions. The eq 8 can thus be written

$$I_{YX} = \alpha_{YX}^2 + \sum \alpha_{IJ}^2 \cdot (C_0, C_1, C_2, A, B, \alpha_{ij}, p_k) \quad (11)$$

The high aperture objective induced reasonably weak scrambling

polarization effects, so in a first approximation, \mathbf{I}_{YX} can be reduced to α_{YX}^2 in our experimental conditions.

Background Light. Despite the use of a Notch filter to eliminate the elastic and low-frequency inelastic contributions of the scattered light collected by the microscope objective, no flat baseline was observed with the fine powdered samples used. Several sources of such backgrounds were previously described.^{49,50} This background light of fine crystal powders was attributed to residual inelastic scattering and/or impurity weak fluorescence emission. The scattering coefficients are approximately inversely proportional to the size of the particles.⁵¹

Software and Data Analysis. Data analysis was performed on a PC, AMD Athlon 1.3 GHz, 768 MB of RAM, running Microsoft Windows version 2000 Professional. All Simplisma X (X has been added to indicate the new version) algorithms were implemented in Matlab version 6.0 software package (MathWorks Inc., Matick, MA). These algorithms use a few scripts from the Chemometrics Toolbox and the Signal Processing Toolbox. The derivative calculations were made in the Simplisma X environment using a mat script called I2ndder written and supplied in the Simplisma X package.

Simplisma Approach. Pure Variable Approach. The principle behind the pure variable approach is that the intensity at a pure variable provides an estimate of the concentration of its associated component. As a consequence, the pure variable intensities can be used as a concentration estimate.

In the present study, the Raman scattering intensity at a wavenumber does not represent the concentration but the orientational function with respect to the Euler angles between the α_{IJ} Raman tensor and the α_{ij} polarizability tensor of the crystal.

$$\mathbf{D} = \mathbf{O} \cdot \mathbf{S}^T + \mathbf{E} \quad (12)$$

\mathbf{D} represents the original data matrix with the spectra in rows, and \mathbf{O} is assumed to be p_k^2 -dependent as defined in eqs 10 and 11. This aspect will be explained in the results section for each sample. \mathbf{O} represents the “orientational function” matrix obtained by using the columns of \mathbf{D} . \mathbf{S} represents the matrix with the squares of polarizability invariants of the crystal ($\Sigma\alpha_{\text{ij}}$) as defined in eq 9 in its columns. \mathbf{S}^T is the transpose of \mathbf{S} . \mathbf{E} represents the residual error, which is minimized in the least squares equations shown below. When the matrixes \mathbf{D} and \mathbf{O} are known (\mathbf{O} becomes known through the Simplisma algorithm), the estimate $\hat{\mathbf{S}}$ of the pure Raman invariants \mathbf{S} can be calculated by standard matrix algebra.

$$\hat{\mathbf{S}} = \mathbf{D}^T \cdot \mathbf{O} \cdot (\mathbf{O}^T \cdot \mathbf{O})^{-1} \quad (13)$$

In a next step, the contributions are now calculated from $\hat{\mathbf{S}}$, which is basically a projection of the original pure variable intensities in the original data set. This step reduces the noise in the contributions. The equation is

$$\mathbf{O}^* = \mathbf{D} \cdot \hat{\mathbf{S}} \cdot (\hat{\mathbf{S}}^T \cdot \hat{\mathbf{S}})^{-1} \quad (14)$$

where \mathbf{O}^* stands for the projected \mathbf{O} .

Because matrix \mathbf{O} does not contain orientational functions but intensities proportional to orientational functions, scaling procedures such as normalization of the resulting spectra in $\hat{\mathbf{S}}$ and the associated inverse normalization of \mathbf{O} are often used for the quantitative information we refer to as the contributions of the components. The data set can be reconstructed as follows:

$$\mathbf{D}^{\text{reconstructed}} = \mathbf{O}^* \cdot \hat{\mathbf{S}}^T \quad (15)$$

The original data set \mathbf{D} and the reconstructed data set $\mathbf{D}^{\text{reconstructed}}$ should be very similar when the proper number of components has been determined. The equation for the difference used here, the relative root of sum of square differences (r) is as follows:

$$r = \sqrt{\frac{\sum_{i=1}^{\text{nspec}} \sum_{j=1}^{\text{nvar}} (d_{ij} - d_{ij}^{\text{reconstructed}})^2}{\sum_{i=1}^{\text{nspec}} \sum_{j=1}^{\text{nvar}} d_{ij}^2}} \quad (16)$$

where d_{ij} is the i th row and j th column element of \mathbf{D} , $d_{ij}^{\text{reconstructed}}$ is the i th row and j th column element of $\mathbf{D}^{\text{reconstructed}}$, nspec is the number of polarization spectra, and nvar is the number of recorded intensities. The value expresses the difference with respect to the original data intensities. For a perfect match, the value is 0.

Pure Variable Selection. A key feature is the purity spectrum, which displays the purity of all of the variables in the spectrum. The maximum is the pure variable. The purity spectrum needs to be corrected for previously selected pure variables. The mathematical formulation is

$$p_{kj} = w_{kj} \cdot \frac{\sigma_j}{\mu_j + \text{off}} \quad (17)$$

where p_{kj} is the j th element of the k th purity spectrum, w_{kj} is a determinant-based weight function,³ and off is an offset to avoid dividing by zero and to bias the purity slightly toward variables with a higher intensity. Typical values for off are 3% of the maximum value in the mean spectrum and 10% for the derivative approach. σ_j and μ_j are the standard deviation and mean of variable j , respectively. The algorithm for pure variables in Simplisma is described in detail elsewhere.^{3,4,9}

Inverted Second Derivative Spectra. In the case of using the second derivative approach in Simplisma, the conventional (in contrast to second derivative) data are used in \mathbf{D} . However, columns of \mathbf{C} consist of intensities from “inverted second derivative data”.

To eliminate baselines, the inverted second derivative spectra are used for Simplisma. The calculation of the inverted second derivatives of spectra lies on the Savitzky–Golay⁵² method and has been described elsewhere.^{5,6} From now on, the term second derivative will be used instead of the inverted second derivative.

Combination of the Use of Conventional and Inverted Second Derivative Data Sets. For the different cases presented here, neither the conventional nor the second derivative approach alone can resolve these data sets. To resolve such data sets properly, Simplisma has been extended toward resolving spectral data using a combination of conventional and second derivative data.¹³ Both the conventional (for pure variables of wide peaks) and the second derivative spectra (for pure variables of narrow peaks, overlapping with wide peaks) are used. This new approach is able to resolve spectra with wide and narrow peaks properly and minimizes baseline problems by resolving them as separate components. For more details about this extension of the Simplisma approach, see ref 13.

Results

The crystal powders used in the present work have been chosen for their relative abundance in atmospheric inorganic matter. Their previously recorded polarized Raman spectra using large oriented single crystals are essential for extensive inter-



Figure 3. Optical image of CaSO_4 crystal analyzed. The framed region is the area in which the Raman spectra were recorded.

pretation of the resolved spectra by the Simplisma approach. Figure 2 shows a schematic picture of the relative size and orientation of microcrystals with respect to the spot size and orientation of the laser focused by large aperture objectives. As detailed in the Experimental Section, the data acquisition consisted of an automatic recording of many spectra in the point-by-point mapping mode with $1\ \mu\text{m}$ as a minimum step with the I_{YX} or I_{XX} polarization set up; see eq 7. Under our experimental conditions, the XY lateral resolution is close to $0.6\ \mu\text{m}$. Because of the roughness of crystals, an automatic focusing objective (Z) at each point was used. Under confocal conditions, the depth of sample seen by the detector is estimated to be $1\ \mu\text{m}$ and corresponds to the Z axial resolution. The spectral and processed data exhibited are typical of several attempts made with I_{YX} or I_{XX} polarization set up.

CaSO_4 . Small crystals of anhydrite were used after grinding of natural crystals. The crystal powder was spread on a microscope glass strip without any further preparation and mounted on the XY microscope stage (Figure 3).

The conventional and second derivative data of a set of 160 spectra recorded in the region of the internal SO_4^{2-} vibrations ($400\text{--}1200\ \text{cm}^{-1}$) with the I_{YX} polarization configuration were treated using the new Simplisma approach without any preprocessing step. The offset is set to 3%. The analysis results in the selection of one conventional pure variable at $1195\ \text{cm}^{-1}$ and five second derivative pure variables. The first pure variable at $1195\ \text{cm}^{-1}$ corresponds to a background spectrum probably caused by inelastic scattering or weak impurity fluorescence. This wavenumber value does not correspond to one of the Raman peaks observed in the conventional data. The correction of the purity spectrum for this first pure variable yields a new purity spectrum without any background anymore. The remaining signal to be treated originates only from Raman scattering signals. That is the reason that the five next pure variables are selected from the second derivative data in the successive selection steps. The following pure variable proposed by the program, $625\ \text{cm}^{-1}$ (in bold in Figure 4a, left column), is therefore selected. The third, fourth, fifth, and sixth ones are consecutively selected (1128 , 608 , 415 , and $497\ \text{cm}^{-1}$, respectively, in bold in Figure 4, left column).

No more spectral information remains once the six pure variables have been selected. As a consequence, this analysis yields one background spectrum and five Raman spectra corresponding to the internal SO_4^{2-} vibrations in CaSO_4 . The relative root of sum of square differences (r , eq 16) between the original data set **D** and the reconstructed data **D**^{reconstructed} is found to be reasonably small (8%) but revealed some polarization scrambling. The left column of Figure 4 shows the resolved

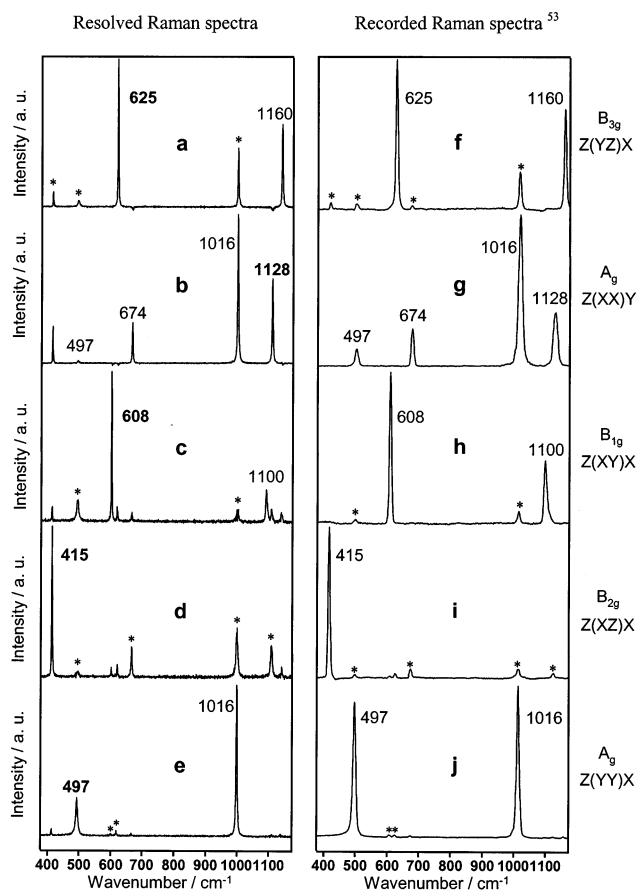


Figure 4. Left column of spectra (parts a–e): series of resolved Raman spectra using the Simplisma approach. Bold peak labels correspond to the respective variables (wavenumbers) selected from the second derivative data during the resolution of the experimental data set. Right column of spectra (parts f–j): polarized Raman spectra of anhydrite as recorded by Berenblut et al.⁵³ Notations under each of the modes irreducible representations to which the spectra are assigned are those of Porto et al.⁵⁷

Raman spectra obtained by the Simplisma approach after having selected the variables bold-labeled. The right column of Figure 4 displays the polarized Raman spectra of oriented single crystals previously published.⁵³ Isolation of the square tensor elements α_{xx}^2 and α_{yy}^2 , α_{xy}^2 , α_{xz}^2 , and α_{yz}^2 by the orientation of the xyz single crystal axes with respect to the XYZ space-fixed coordinates of a conventional Raman apparatus leads to the isolation of A_g , B_{1g} , B_{2g} , and B_{3g} Raman active modes, respectively.

The Simplisma analysis of simulated spectra obtained by random linear combination of the polarized spectra of oriented single crystals permits us to extract accurate polarized spectra with a very low r value (0.00%). This finding demonstrates the ability of the Simplisma approach to extract significant spectra from the data set. The weak unexpected peaks observed in the resolved spectra arise probably from polarization scrambling. It should be noted that the Raman peaks star-labeled in the spectra of the left column of Figure 4 were previously observed as polarization leakage in polarized spectra of the right column.⁵³ Scanning over a given set of n crystallites assumed to be randomly oriented supplies a set of (θ, ϕ, χ) angles and thus a set of \mathbf{O}_k varying functions for eq 12. This induces varying relative intensities **D** in eq 12 of the 160 recorded Raman spectra. The Simplisma analysis of this spectral data set provides five **S**-resolved Raman spectra.

The **S**-extracted spectra can be interpreted by the use of eq 12, taking the position of the crystal-fixed coordinate system *xyz* positioned relative to the *XYZ* frame thanks to the θ , ϕ , χ Euler angles into account, as indicated in Figure 2.

The Raman scattering tensors of the anhydrite crystal are⁵⁴

$$\alpha_{xyz}^{A_g} = \begin{pmatrix} a & 0 & 0 \\ 0 & b & 0 \\ 0 & 0 & c \end{pmatrix} \quad (18)$$

$$\alpha_{xyz}^{B_{1g}} = \begin{pmatrix} 0 & d & 0 \\ d & 0 & 0 \\ 0 & 0 & 0 \end{pmatrix} \quad (19)$$

$$\alpha_{xyz}^{B_{2g}} = \begin{pmatrix} 0 & 0 & e \\ 0 & 0 & 0 \\ e & 0 & 0 \end{pmatrix} \quad (20)$$

$$\alpha_{xyz}^{B_{3g}} = \begin{pmatrix} 0 & 0 & 0 \\ 0 & 0 & f \\ 0 & f & 0 \end{pmatrix} \quad (21)$$

There are large differences in relative intensities of the several allowed A_g modes from element to element. It was found that the relative intensities of the α_{yy} and α_{zz} spectra were almost identical ($\alpha_{yy} \sim \alpha_{zz} = b$) but that the $\alpha_{xx} = a$ spectrum was quite different. At a given wavenumber $\bar{\nu}$, one deduces from eqs 10 and 11 that the different contributions A_g , B_{1g} , B_{2g} , and B_{3g} to the function $I_{YX} \propto \alpha_{YX}^2$ are

$$I_{YX}(\bar{\nu}) = (b - a)^2 \cdot (p_1 - p_2)^2 + d^2 \cdot p_3^2 + e^2 \cdot p_4^2 + f^2 \cdot p_5^2 \quad (22)$$

The $(p_1 + p_2)^2$, p_3^2 , p_4^2 , and p_5^2 theoretical orientational functions of the θ , ϕ , χ Euler angles can be identified as the O_1 , O_2 , O_3 , and O_4 varying functions in Simplisma, respectively; see eq 11. In the same way, $(b - a)^2$, d^2 , e^2 , and f^2 functions of the crystal Raman tensor can be identified as the five **S** pure spectra resolved by Simplisma. The comparison between the five extracted Raman spectra of crystal powder of anhydrite and the five polarized Raman spectra of oriented anhydrite single crystal previously published, Figure 4, indicates clear analogies in wavenumber and relative intensities of the Raman peaks. This finding demonstrates the ability of Simplisma to extract specific contributions of A_g , B_{1g} , B_{2g} , and B_{3g} Raman active modes of crystal powder spectral set. However, the relative intensities of the A_g modes differ somewhat from those obtained by the isolation of the crystal tensor element by the orientation of the *xyz* single crystal axes with respect of the fixed coordinates *XYZ*.

From the Raman data set recorded from crystal powder of anhydrite, five spectra were isolated by the Simplisma approach. These spectra correspond to specific contributions of A_g , B_{1g} , B_{2g} , and B_{3g} Raman active modes of crystal.

CaCO₃. First, the data acquisition was performed by recording many spectra of fine crystal powder of calcite with particle size less than 1 μm being aggregates of many crystallites. The Simplisma analysis of the 360 spectra results in the selection of a conventional pure variable at 1201 cm^{-1} and three second derivative pure variables at 1086, 282, and 713 cm^{-1} . After many attempts, this analysis yields only one Raman spectrum with four peaks corresponding to the well-known CaCO_3 powder spectrum with a weak baseline (Figure 5). The *r* value was found to be reasonable (5.7%).

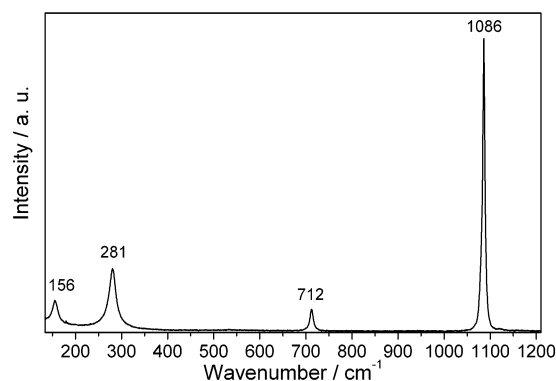


Figure 5. Raman spectrum of fine calcite powder resolved by the Simplisma approach.

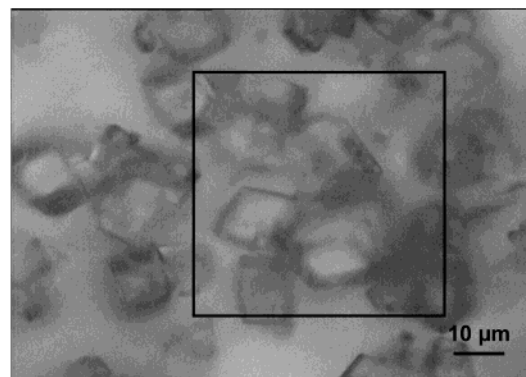


Figure 6. Optical image of CaCO_3 crystals analyzed. The framed region is the area in which the Raman spectra were recorded.

Second, data collection were carried out with coarse crystal powders (average crystal size $\sim 7 \mu\text{m}$) (Figure 6). The conventional and second derivative spectra of a set of 625 spectra recorded in the internal and external CO_3^{2-} vibration wavenumber region (100–1200 cm^{-1}) with the I_{YX} polarization configuration were treated using Simplisma. The offset was set to 3%. The analysis results in the selection of one conventional pure variable at 1186 cm^{-1} and three second derivative pure variables at 1086, 282, and 713 cm^{-1} . The resolved spectrum with conventional first pure variable at 1186 cm^{-1} corresponds to the Raman spectrum of fine powder and weak baseline caused by inelastic scattering. The correction of the purity spectrum for this first pure variable yields a new purity spectrum with a flat background. No other spectral information remains once the four pure variables are selected.

As a consequence, this analysis yields one background spectrum and three Raman spectra corresponding to the internal CO_3^{2-} vibrations in CaCO_3 (Figure 7). The *r* value is found to be reasonable (9%) when considering the size of the data set (625 spectra \times 2042 intensities = 1 276 250 data) but revealed some scrambling, which may be due to high birefringence of calcite and nonspecific orientational functions.

The scattering tensors are

$$\alpha_{xyz}^{A_{1g}} = \begin{pmatrix} a & 0 & 0 \\ 0 & a & 0 \\ 0 & 0 & b \end{pmatrix} \quad (23)$$

$$\alpha_{xyz}^{E_g} = \begin{pmatrix} c & -c & -d \\ -c & -c & d \\ -d & d & 0 \end{pmatrix} \quad (24)$$

At a given wavenumber $\bar{\nu}$, one deduces from eqs 10 and 11 the

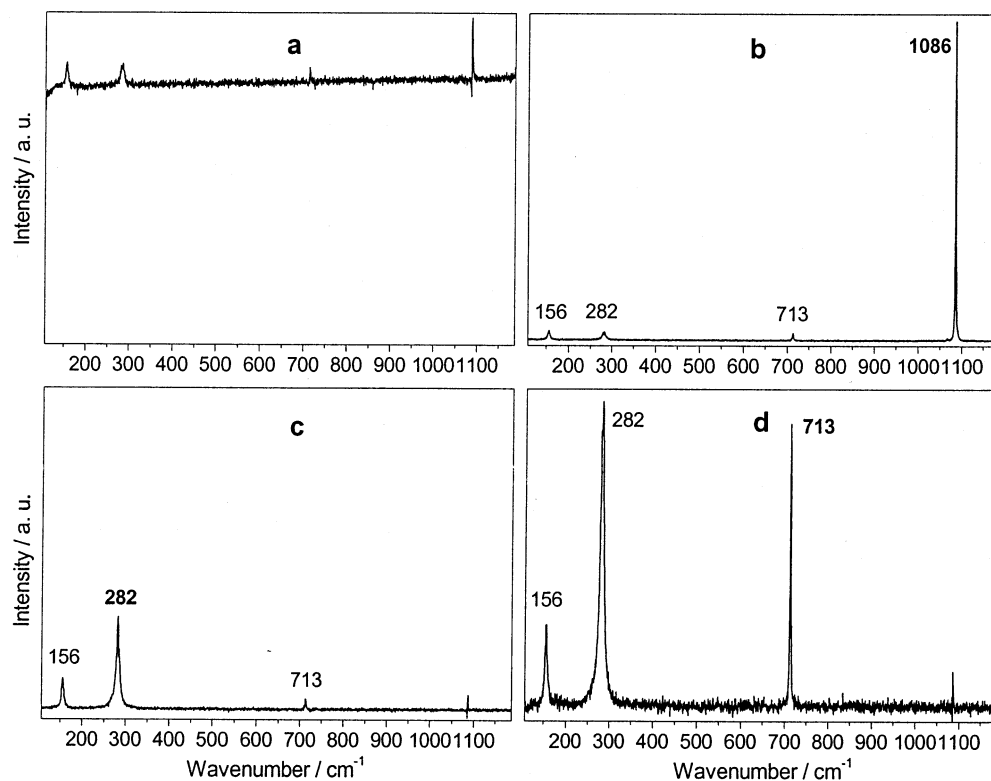


Figure 7. Raman spectra resolved from spectra of crystalline CaCO_3 using the Simplisma approach. (a) Raman spectrum resolved subsequently to the selection of the variable 1186 cm^{-1} in the conventional data. (b–d) Bold peak labels correspond to the respective variables (wavenumbers) selected for the resolution of the experimental data.

different contributions A_{1g} and E_g to the function $I_{YX} \propto \alpha_{YX}^2$

$$I_{YX}(A_{1g}, \bar{\nu}) \propto (b - a)^2 \cdot p_1^2 \quad (25)$$

$$I_{YX}(E_g, \bar{\nu}) \propto c^2 \cdot (2p_2 + p_3)^2 + d^2 \cdot (p_4 + p_5)^2 - 2cd \cdot (2p_2 + p_3) \cdot (p_4 + p_5) \quad (26)$$

$I_{YX} \propto \alpha_{YX}^2$ can thus be rewritten into

$$I_{YX}(\bar{\nu}) = (b - a)^2 \cdot p_1^2 + c^2 \cdot [2p_2 \cdot (2p_2 - p_3) + p_3 \cdot (p_3 - p_4)] + d^2 \cdot [p_5 \cdot (p_5 - 2p_2) + p_4 \cdot (p_4 - p_3)] + (c - d)^2 \cdot [2p_2 \cdot p_5 + p_3 \cdot p_4] \quad (27)$$

The p_1^2 , $[2p_2 \cdot (2p_2 - p_3) + p_3 \cdot (p_3 - p_4)]$, $[p_5 \cdot (p_5 - 2p_2) + p_4 \cdot (p_4 - p_3)]$ and $[2p_2 \cdot p_5 + p_3 \cdot p_4]$ theoretical orientational functions of the θ , ϕ , χ Euler angles are identified as the O_1 , O_2 , O_3 , and O_4 varying functions in Simplisma; see eq 11. In the same way, $(b - a)^2$, c^2 , d^2 or $(c - d)^2$ functions of the crystal Raman tensor element can be identified as the S pure Raman spectra resolved by Simplisma (Figure 7). The comparison between the three extracted Raman spectra of crystal powder of calcite and the polarized Raman spectra of oriented calcite single crystal previously published⁴² indicates clear analogies in wavenumber and relative intensities of the Raman peaks. The S $((b - a)^2)$ -resolved spectrum, Figure 7b, can directly be compared to the $\alpha_{zz}^2 = b^2$ polarized spectrum, which exhibits only one Raman peak at 1086 cm^{-1} assigned to the A_{1g} mode. It should be noted that three very weak peaks (E_g modes) can be detected in the resolved spectrum and in the polarized α_{zz}^2 spectrum as well. The S (c^2) - and S (d^2) -resolved spectra, Figure 7c,d, are analogous to the $\alpha_{xy}^2 = c^2$ and $\alpha_{zx}^2 = d^2$ spectra

isolated by polarization measurements. The spectra contain three Raman peaks assigned to E_g modes, with a very weak feature at 1086 cm^{-1} (A_{1g}). However, some differences can be observed between the relative intensities of the resolved and polarized spectra attributed to interference with the remaining O_4 orientational term of eq 27. Similar results were obtained from medium crystal powders ($1 \mu\text{m}$ average particle size).

From the Raman data set recorded from medium and coarse crystal powders of calcite, four spectra were isolated by the Simplisma approach: a Raman powder spectrum superimposed with weak baseline and three specific contributions of A_{1g} and E_g Raman active modes of crystal. In contrast, from Raman data set recorded with fine crystal powder, only one Raman powder spectrum of calcite was resolved.

$\text{CaSO}_4 \cdot 2\text{H}_2\text{O}$. The Simplisma analysis results in the selection of one conventional pure variable at 791 cm^{-1} and four second derivative pure variables at 493 (A_g), 415 (A_g), 670 (B_g), and 1134 (B_g) cm^{-1} . Figures 8 and 9 show the Raman spectra resolved by Simplisma from a spectral data set (240 spectra) of crystal powder of gypsum. The particle size is approximately $12 \mu\text{m}$ in size and appears as an aggregate of many $1 \mu\text{m}$ crystallites. Variables selected are represented in bold type in Figure 9.

The first conventional pure variable at 791 cm^{-1} corresponds to the Raman spectrum of $\text{CaSO}_4 \cdot 2\text{H}_2\text{O}$ powder and weak baseline caused by inelastic scattering (Figure 8). Polarized Raman spectra resolved from 493 and 415 cm^{-1} variables, respectively, are displayed in Figure 9a,b, while parts c and d show those obtained after the selection of variables 670 and 1134 cm^{-1} . The r value is found relatively high but remains reasonable (7.4%). It corresponds to scrambling, which may be due to nonspecific varying functions O_k in eq 11 because the birefringence of gypsum is weak.

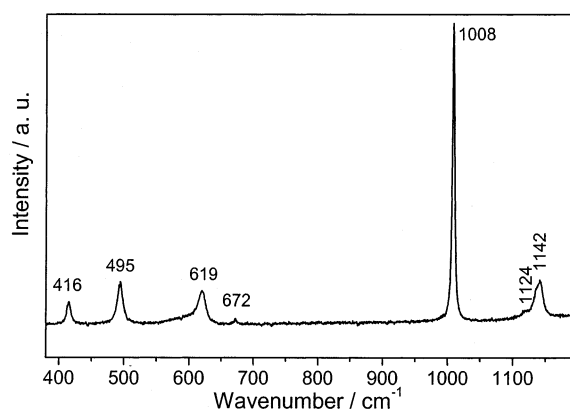


Figure 8. Resolved powder Raman spectrum from spectra of crystalline $\text{CaSO}_4 \cdot 2\text{H}_2\text{O}$ using the Simplisma approach subsequently to the selection of the variable 791 cm^{-1} in the conventional data.

The scattering tensors are of the following forms

$$\alpha_{xyz}^{A_g} = \begin{pmatrix} a & 0 & d \\ 0 & b & 0 \\ d & 0 & c \end{pmatrix} \quad (28)$$

$$\alpha_{xyz}^{B_g} = \begin{pmatrix} 0 & e & 0 \\ e & 0 & f \\ 0 & f & 0 \end{pmatrix} \quad (29)$$

The application of eqs 9 and 10 to A_g and B_g modes leads to

$$\begin{aligned} I_{YX}(A_g, \bar{\nu}) \propto & (2c - a - b)^2 \cdot (p_1^2 - p_1 \cdot p_2 - p_1 \cdot p_4) + \\ & (a - b)^2 \cdot (p_2^2 - p_1 \cdot p_2 - p_2 \cdot p_4) + d^2 \cdot p_4 \cdot (p_4 - p_1) + \\ & 4 \cdot (c - b)^2 \cdot p_1 \cdot p_2 + (a - b + d)^2 \cdot p_2 \cdot p_4 + \\ & (2c - a - b + d)^2 \cdot p_1 \cdot p_4 \quad (30) \end{aligned}$$

and

$$I_{YX}(B_g, \bar{\nu}) \propto e^2 \cdot p_3 \cdot (p_3 - p_4) + f^2 \cdot p_4 \cdot (p_4 - p_3) + (e - f)^2 \cdot p_3 \cdot p_4 \quad (31)$$

The theoretical orientational functions (p_k) of the θ , ϕ , χ Euler angles are identified as the \mathbf{O}_k , varying functions in Simplisma, eq 12 (see Experimental Section). In the same way, the terms (a–f) including the elements of the crystal Raman tensor can be identified as the \mathbf{S}_k Raman spectra resolved by Simplisma, eq 12. The comparison between the resolved \mathbf{S}_k spectra, Figure 9, and the polarized α_{xx} , α_{zz} , α_{xy} , and α_{zy} spectra previously reported,⁴³ indicate some polarization effects in the resolved spectra. However, the relative intensities were found to depend dramatically on the selected pure variable and some A_g Raman features are observed in the B_g spectra, particularly, the most intense mode at 1008 cm^{-1} is extracted. The varying functions \mathbf{O}_k associated with the \mathbf{S}_k extracted spectra do not appear as specific orientational functions of the tensor elements. These characteristics do not permit resolution of the A_g and B_g modes from crystal powder spectra by the Simplisma approach.

From the Raman data set recorded from medium and fine crystal powders of gypsum, several spectra were isolated by the Simplisma approach: a Raman powder spectrum superimposed with weak baseline and several nonspecific contributions of A_g and B_g Raman active modes of the crystal.

$(\text{NH}_4)_2\text{SO}_4$. Raman spectra of $(\text{NH}_4)_2\text{SO}_4$ crystal powder corresponding to crystallites with $1 \mu\text{m}$ average size were recorded in the internal SO_4^{2-} vibrations wavenumber range ($400\text{--}1200 \text{ cm}^{-1}$) as described above. The conventional and second derivative spectra of a set of 114 spectra were treated as already described. The offset was set to 3% of the mean spectrum maximum. The analysis results in the selection of one conventional pure variable at 1176 cm^{-1} and several second derivative pure variables including the Raman 451, 616, 626, 976, and 1061 cm^{-1} . The first conventional pure variable at 1176 cm^{-1} corresponds to the Raman spectrum of $(\text{NH}_4)_2\text{SO}_4$ powder and weak baseline caused by inelastic scattering, and numerous attempts to resolve Raman bands modes generated by static and dynamic crystal effects upon SO_4^{2-} vibrations in $(\text{NH}_4)_2\text{SO}_4$ crystal were carried out.

The resolved spectrum with conventional first pure variable at 1176 cm^{-1} corresponds to the Raman spectrum of $(\text{NH}_4)_2\text{SO}_4$ and weak baseline caused by inelastic scattering (Figure 10a). All of the resolved \mathbf{S}_k Raman spectra (not shown) according to the different second derivative-selected variables were found to be analogous, however, with different relative intensities except for the resolution of two bands at 626 and 616 cm^{-1} (Figure 10b,c). The r value is found to be low (3%) after the six extractions. It should be noted that factor groups of $(\text{NH}_4)_2\text{SO}_4$ and CaSO_4 are identical and belong to D_{2h} . The Raman tensors of $(\text{NH}_4)_2\text{SO}_4$ and anhydrite crystals have identical forms. A critical examination of \mathbf{S}_k -resolved Raman spectra and α_{ij} polarized spectra previously reported reveals that the α_{ii} spectra (A_g) are not sufficiently different from each other and from α_{zy} (B_{1g}), α_{xz} (B_{2g}), and α_{xy} (B_{3g}) in wavenumber as to be resolved by Simplisma. We are unable to select any suitable pure variable to resolve spectra from the data set with some resemblance with the polarized spectra in the relative intensities. In addition, in the polarized spectra, the 976 cm^{-1} mode expected to show one component in each of the A_g and B_{1g} polarized spectra according to group theory is detected in the polarized spectra of B_{2g} and B_{3g} modes. This spillover could result from unavoidable errors in the scattering geometries and imperfections in the crystal.⁵⁵

Discussion

The selected examples shown above demonstrate the ability of the Simplisma approach to resolve more than one Raman spectrum characteristic of a pure crystalline product from spectral data set recorded with a confocal microspectrometer from crystal powder samples. The relative size of the crystalline particles, between less than 0.5 and $10 \mu\text{m}$, and the spot size ($\sim 1 \mu\text{m}$) of the laser focused by the objective at the sample are critical variables from the experimental viewpoint. The fundamental physical phenomenon under this finding is the well-known static and dynamic crystal effects.^{54,56} For example, in the case of CaSO_4 , the SO_4^{2-} ions (point group T_d) occupy one site of lower symmetry, C_{2v} , resulting in a complete removal of degeneracies of the free ion modes. Furthermore, the primitive unit cell is noncentrosymmetric (D_{2h} factor group); thus, there is a splitting of each mode into two components having odd and even normal coordinates with respect to the inversion operation. By the rule of mutual exclusion, the even (g) ones are Raman active while the odd (u) ones are infrared active. There are not only changes in the number of bands and wavenumbers but also changes in Raman intensities.^{54,56} The collected Raman scattering can be considered as the contribution of several Raman tensor elements according to the symmetry of the vibration modes. The Raman powder sample spectra are

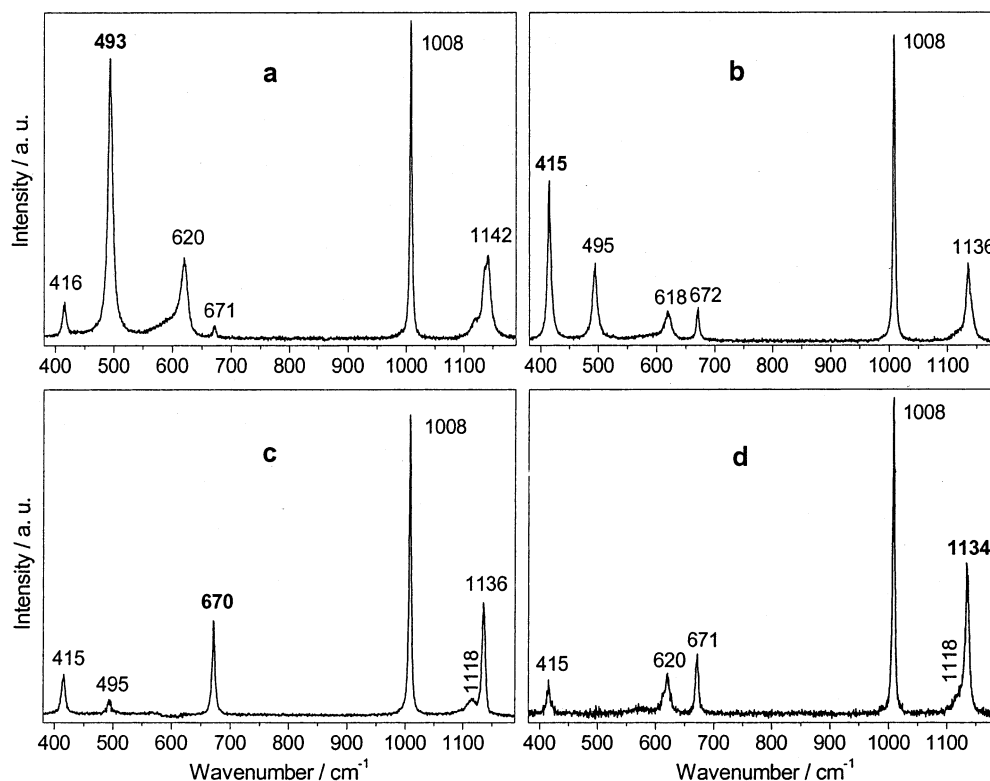


Figure 9. Raman spectra resolved from spectra of crystalline $\text{CaSO}_4 \cdot 2\text{H}_2\text{O}$ using the Simplisma approach. Bold peak labels correspond to the respective variables (wavenumbers) selected in the second derivative data set for the resolution of the experimental data.

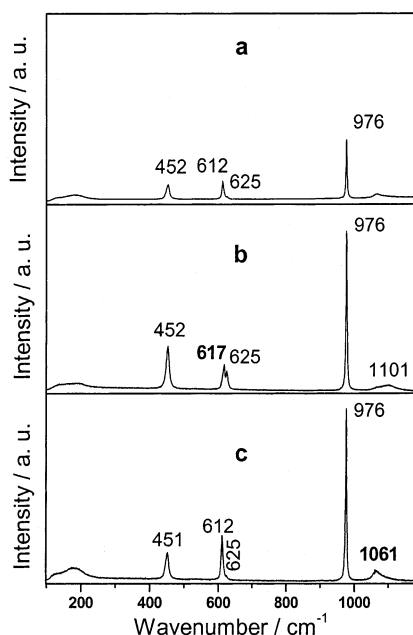


Figure 10. Raman spectra resolved from spectra of crystalline $(\text{NH}_4)_2\text{SO}_4$ using the Simplisma approach. (a) Powder Raman spectrum resolved subsequently to the selection of the variable 1176 cm^{-1} in the conventional data. (b,c) Bold peak labels correspond to the respective variables (wavenumbers) selected in the second derivative data set for the resolution of the experimental data. The three spectra are scaled to the same maximum intensity.

typically recorded with conventional Raman or FT-Raman instruments with a laser focalization spot (1 mm) larger than the crystal size (less than $10\text{ }\mu\text{m}$) of the powder sample, so the random orientation of crystallites leads to an average contribution of several Raman tensor elements to the Raman scattering. Often, highly overlapping spectral features and baselines are

present in the powder spectra. An account for the Raman and baseline intensities of powder samples has been given previously as an extension of the theory due to Kubelka and Munk.⁵¹

The isolation of the $\alpha_{ij}(\bar{\nu})$ tensor elements by linearly polarized Raman scattering measurements of large single crystals oriented with respect to the direction and polarization of the exciting and scattered lights leads to the isolation of Raman modes according to their vibrational symmetry. The Raman band intensity is proportional to the $\alpha_{ij}^2(\bar{\nu})$ value. The variation of the orientation of the crystal with respect to space-fixed coordinates of the instrument causes variations of the relative Raman band intensities. This variance parameter through the Euler angle functions has been used by the Simplisma approach in the present work to resolve spectra representative of individual $\alpha_{ij}^2(\bar{\nu})$ tensor element or combinations. Second derivative spectra can be used to resolve the data properly. The new Simplisma approach based on a combination of conventional and second derivative data has been used to resolve the data properly.

When Raman spectra of crystal powder are recorded with a microspectrometer, the focused laser spot size ($1\text{ }\mu\text{m}$) can be in the range of the crystal size. The random orientation of the crystal faces with respect to the laser beam and polarization direction and the motorized data acquisition produce large amounts of spectral data by point-by-point scanning with a significant variance. The Simplisma analysis first results in the selection of conventional pure variable characteristic of the baseline to extract the background. The concomitant extraction of baseline and powder Raman spectra indicates some simultaneous variance of inelastic diffuse scattering and Raman scattering of fine particles (Figures 5, 8, and 10a). The further selection of Raman second derivative pure variables allows construction of several Raman spectra, which are compared to the polarized Raman spectra recorded previously with large single crystal using conventional instruments. The analogies between the corresponding, polarized, and Simplisma-resolved

spectra of CaSO_4 and CaCO_3 are accurately explained through theoretical equations taking into account the Raman tensor elements of crystal and orientational functions defining the orientation of the crystal-fixed coordinates with respect to the space-fixed coordinates. The Raman intensity variations do not depend on the concentration as expected for the use of Simplisma but on the crystal orientation. In the case of $(\text{NH}_4)_2\text{SO}_4$, the weak static and dynamic crystal effects generate too weak Raman band splittings to be resolved through the Simplisma analysis even with the second derivative variables. In contrast, in the case of $\text{CaSO}_4 \cdot 2\text{H}_2\text{O}$, the Raman tensor forms do not allow the definition of specific orientational functions to extract spectra directly comparable to the polarized spectra. In all cases, the presence of powder crystal as very fine particles leads to the resolution of one Raman spectrum identical to those previously reported.

The polarization scrambling induced by the optical properties of the crystal and the depolarization effect of the high aperture objective can be minimized by the high spatial resolution given by the confocal conditions. These conditions are ascertained by the use of an autofocusing system and the point-by-point mode of spectra recording. The polarization scrambling of the high aperture objective through the C_0 , C_1 , C_2 , A , and B correction coefficients are minimized by the Simplisma processing. In eq 11, the correction terms $\sum \alpha_{ij}^2$ contributions are not theoretically extracted by the selection of the pure variables in the limit of the orientational functions; p_k are different from p_1 , p_2 , p_3 , p_4 , and p_5 functions in α_{YX}^2 . Nevertheless, the birefringence induces polarization scrambling, which contributes to the residue (r value).

Conclusions

The analyses by confocal Raman microspectrometry in point-by-point scanning mode of samples with heterogeneity larger than the spatial resolution ($\sim 1 \mu\text{m}$) generate large amounts of Raman spectral data. As recently reported, it is clear that the data processing using the Simplisma approach provides exhaustive species identification and molecular imaging of complex media. The present selected examples of fine, medium, and coarse crystal powders treated by the new Simplisma method demonstrate the main role of the crystal size on the number and shape of the resolved spectra. With fine crystal powders (size less than $0.5 \mu\text{m}$), well-known powder Raman spectrum characteristics of each compound were extracted. This spectrum was often superimposed with a weak baseline. With medium and coarse crystal powders (size more than $1 \mu\text{m}$), several significant spectra were extracted for each pure crystalline compound. These spectra were found to be analogous to the polarized spectra obtained with oriented large single crystals and attributed to the several scattering contributions according to the symmetry of the several vibrational modes. The band splittings by the static and dynamic crystal effects can be resolved by the Simplisma approach according to the width of the splitting and the crystal space group. These results were explained by theoretical equations deduced from the Raman tensor elements and orientational functions of the crystal-fixed coordinates with respect to the space-fixed coordinates. These findings could lead to molecular orientational order imaging of materials with large heterogeneity.

Acknowledgment. We thank Dr. S. Sobanska, Laboratoire de Spectrochimie Infrarouge et Raman of the Université des Sciences et Technologies de Lille, for natural anhydrite crystals. We are most grateful to the Région Nord-Pas de Calais and the

“Fonds Européen de Développement Economique des Régions” for financial support of the concerted research program (PRC). The Centre d'Etude et de Recherches Laser et Applications (CERLA) is supported by the “Ministère chargé de la recherche”, the “Région Nord-Pas de Calais”, and the “Fonds Européen de Développement Economique des Régions”.

References and Notes

- (1) Hamilton, J. C.; Gemperline P. J. *J. Chemom.* **1990**, *4*, 1–13.
- (2) Windig, W. *Chemom. Intell. Lab. Syst.* **1992**, *16*, 1.
- (3) Windig, W.; Guilment, J. *Anal. Chem.* **1991**, *63*, 1425.
- (4) Windig, W.; Heckler, C. E.; Agblevor, F. A.; Evans, R. J. *Chemom. Intell. Lab. Syst.* **1992**, *14*, 195.
- (5) Windig, W.; Stephenson, D. A. *Anal. Chem.* **1992**, *64*, 2735.
- (6) Windig, W. *Chemom. Intell. Lab. Syst.* **1994**, *23*, 71.
- (7) Windig, W.; Markel, S. J. *Mol. Struct.* **1993**, *292*, 161.
- (8) Guilment, J.; Markel, S.; Windig, W. *Appl. Spectrosc.* **1994**, *48*, 320.
- (9) Windig, W. *Chemom. Intell. Lab. Syst.* **1997**, *36*, 3.
- (10) Vacque, V.; Dupuy, N.; Sombret, B.; Huvenne J. P.; Legrand, P. *Appl. Spectrosc.* **1997**, *51*, 407.
- (11) Batonneau, Y.; Brémard, C.; Laureyns, J.; Merlin, J. C. *J. Raman Spectrosc.* **2000**, *31*, 1113.
- (12) Batonneau, Y.; Laureyns, J.; Merlin, J. C.; Brémard, C. *Anal. Chim. Acta* **2001**, *446*, 23.
- (13) Windig, W.; Antalek, B. J.; Lippert, J. L.; Batonneau, Y.; Brémard, C. *Anal. Chem.* **2002**, *74*, 1371.
- (14) Moissette, A.; Gener, I.; Brémard, C. *J. Phys. Chem. B* **2001**, *105*, 5647.
- (15) Moissette, A.; Brémard, C. *Microporous Mesoporous Mater.* **2001**, *47*, 345.
- (16) Moissette, A.; Batonneau, Y.; Brémard, C. *J. Am. Chem. Soc.* **2001**, *123*, 12325.
- (17) Phalp, J. M.; Payne, A. W.; Windig, W. *Anal. Chim. Acta* **1995**, *318*, 43.
- (18) Toft, J.; Cuesta-Sanchez, F.; van den Bogaert, B.; Libnau, F. O.; Massart, D. L. *Vib. Spectrosc.* **1996**, *10*, 125.
- (19) Mansuetto, E. S.; Wight, C. A. *Appl. Spectrosc.* **1992**, *46*, 1799.
- (20) Sasic, S.; Ozaki, Y.; Olinga, A.; Siesler, H. W. *Anal. Chim. Acta* **2002**, *452*, 265.
- (21) Cuesta Sanchez, F.; Toft, J.; van den Bogaert, B.; Massart, D. L.; Dive, S. S.; Hailey, P. *Fresenius' J. Anal. Chem.* **1995**, *352*, 771.
- (22) Sasic, S.; Segtnan, V. H.; Ozaki, Y. *J. Phys. Chem. A* **2002**, *106*, 760.
- (23) Verberckmoes, A. A.; Weckhuysen, B. M.; Schoonheydt, R. A. In *Progress in Zeolite and Microporous Materials/Studies in Surface Science and Catalysis*; Chon, H., Ihm, S.-K., Uh, Y. S., Eds.; Elsevier Science: New York, 1997; Vol. 105, p 623.
- (24) Gener, I.; Moissette, A.; Brémard, C. *Chem. Commun.* **2000**, *17*, 1563.
- (25) Verberckmoes, A. A.; Weckhuysen, B. M.; Schoonheydt, R. A.; Ooms, K.; Langhans, I. *J. Mol. Catal. A* **2000**, *151*, 115 and references therein.
- (26) Gargallo, R.; Cuesta-Sanchez, F.; Izquierdo-Ridorsa, A.; Massart, D. L. *Anal. Chem.* **1996**, *68*, 2241.
- (27) Brémard, C.; Buntinx, G.; de Waele, V.; Didierjean, C.; Gener, I.; Poizat, O. *J. Mol. Struct.* **1999**, *480–481*, 69.
- (28) Esteves da Silva, J. C. G.; Machado, A. A. S. C.; Oliveira, C. J. S.; Pinto, M. S. S. D. *Talanta* **1998**, *45*, 1155 and references therein.
- (29) Smith, D. S.; Kramer, J. R. *Anal. Chim. Acta* **2000**, *416*, 211.
- (30) Shin, H. S.; Hong, K. H.; Lee, M. H.; Cho, Y. H.; Lee, C. W. *Talanta* **2001**, *53*, 791.
- (31) Esteves da Silva, J. C. G.; Machado, A. A. S. C.; Ferreira, M. A.; Rey, F. *Can. J. Chem.* **1998**, *76*, 1197.
- (32) Smith, D. S.; Kramer, J. R. *Environ. Int.* **1999**, *25*, 295.
- (33) Buxton, T. L.; Harrington, P. D. *Anal. Chim. Acta* **2001**, *434*, 269 and references therein.
- (34) Harrington, P. B.; Rauch, P. J.; Cai, C. S. *Anal. Chem.* **2001**, *73*, 3247 and references therein.
- (35) Artyushkova, K.; Fulghum, J. E. *J. Electron Spectrosc. Relat. Phenom.* **2001**, *121*, 33.
- (36) Brémard, C.; Dhamelincourt, P.; Laureyns, J.; Turrell, G. *Appl. Spectrosc.* **1985**, *39*, 1036.
- (37) Lagugné Labarthe, F.; Buffeteau, T.; Sourisseau, C. *J. Phys. Chem. B* **1998**, *102*, 5754.
- (38) Lagugné Labarthe, F.; Bruneel, J. L.; Sourisseau, C.; Huber, M. R.; Börger, V.; Menzel, H. J. *Raman Spectrosc.* **2001**, *32*, 665 and references therein.
- (39) Jen, S.; Clark, N. A.; Pershan, P. S.; Priestley, E. B. *J. Chem. Phys.* **1977**, *66*, 4635.

- (40) Miyano, K. *J. Chem. Phys.* **1978**, 69, 4807.
- (41) Davies, A. N.; Jones, J. W.; Price, A. H. *J. Raman Spectrosc.* **1994**, 25, 521.
- (42) Porto, S. P. S.; Giordmaine, J. A.; Damen, T. C. *Phys. Rev.* **1966**, 147, 608 and references therein.
- (43) Berenblut, B. J.; Dawson, P.; Wilkinson, G. R. *Spectrochim. Acta* **1971**, 27A, 1849.
- (44) Turrell, G. *J. Raman Spectrosc.* **1984**, 15, 103.
- (45) Brémard, C.; Laureyns, J.; Merlin, J. C.; Turrell, G. *J. Raman Spectrosc.* **1987**, 18, 305.
- (46) Brémard, C.; Laureyns, J.; Turrell, G. *Can. J. Spectrosc.* **1987**, 32, 70.
- (47) Brémard, C.; Laureyns, J.; Turrell, G. *J. Chim. Phys.* **1989**, 86, 1245.
- (48) Wilson, E. B., Jr.; Decius, J. C.; Cross, P. C. In *Molecular Vibrations the Theory of Infrared and Raman Vibrational Spectra*; Dover Publications, Inc.: New York, 1980; pp 285–286.
- (49) Schrader, B.; Bergmann, B. Z. *Anal. Chem.* **1967**, 225, 230.
- (50) Schrader, B.; Hoffmann, A.; Keller, S. *Spectrochim. Acta* **1991**, 47A, 1135.
- (51) Waters, D. N. *Spectrochim. Acta* **1994**, 50A, 1833.
- (52) Savitzky, A.; Golay, M. J. E. *Anal. Chem.* **1964**, 36, 1627.
- (53) Berenblut, B. J.; Dawson, P.; Wilkinson, G. R. *Spectrochim. Acta* **1973**, 29A, 29.
- (54) Turrell, G. *Infrared and Raman Spectra of Crystals*; Academic Press: London, 1972.
- (55) Venkateswarlu, P.; Bist, H. D.; Jain, Y. S. *J. Raman Spectrosc.* **1975**, 3, 143.
- (56) Decius, J. C.; Hexter, R. M. *Molecular Vibrations in Crystals*; McGraw-Hill International Book Company: New York, 1977.
- (57) Damen, T. C.; Porto, S. P. S.; Tell, B. *Phys. Rev.* **1966**, 144, 771.